High-precision laser beam shaping using a binary-amplitude spatial light modulator

Jinyang Liang,[1,*] Rudolph N. Kohn, Jr.,[2] Michael F. Becker,[1] and Daniel J. Heinzen[2]

[1]Department of Electrical and Computer Engineering, University of Texas at Austin, Austin, Texas 78712, USA

[2]Department of Physics, University of Texas at Austin, Austin, Texas 78712, USA

*Corresponding author: jinyang.liang@mail.utexas.edu

We have achieved high-precision laser beam shaping by using a binary-amplitude spatial light modulator, a digital micromirror device (DMD), followed by an imaging telescope that contains a pinhole low-pass filter (LPF). An error diffusion algorithm was used to design the initial DMD pixel pattern based on the measured input beam profile. This pattern was iteratively refined by simulating the optically low-pass filtered DMD image and changing DMD pixels to lift valleys and suppress peaks. We noted the gap between the experimental result of 1.4% root-mean-square (RMS) error and the simulated result for the same DMD pattern of 0.3% RMS error. Therefore, we deemed it necessary to introduce iterative refinement based on actual measurements of the output image to further improve the uniformity of the beam. Using this method, we have demonstrated the ability to shape raw, non-spatially filtered laser beams (quasi-Gaussian beams) into beams with precisely controlled profiles that have an unprecedented level of RMS error with respect to the target profile. We have shown that our iterative refinement process is able to improve the light intensity uniformity to around 1% RMS error in a raw camera image for both 633 and 1064 nm laser beams. The use of a digital LPF on the camera image is justified in that it matches the performance of the pinhole filter in the experimental setup. The digital low-pass filtered results reveal that the actual optical beam profiles have RMS error down to 0.23%. Our approach has also demonstrated the ability to produce a range of target profiles as long as they have similar spatial-frequency content (i.e., a slowly varying beam profile). Circular and square cross-section flat-top beams and beams with a linear intensity variation within a circular and square cross section were produced with similarly low RMS errors. The measured errors were about twice the ultimate limit of 0.1% RMS error based on the number of binary DMD pixels that participate in the beam-formation process.   © 2010 Optical Society of America

OCIS codes: 070.6120, 140.3300, 230.6120.

1. Introduction

Laser beams with precisely controlled intensity profiles are essential for many areas of optics and optical physics. Control of the beam intensity profile to less than 1% root-mean-square (RMS) error is needed for a number of select applications. In optical physics, for example, flat-top beams could improve the sensitivity of interferometric gravity wave detectors [1]. A flat-top beam is defined as a laser beam with a central region of uniform irradiance surrounded by a region in which irradiance goes to zero as radius increases. Ultracold atoms loaded into optical lattices have important applications, including optical lattice atomic clocks [2] and quantum emulation [3]. Optical lattices are formed by standing wave interference of single-mode laser beams, usually of Gaussian transverse profile, and ultracold atoms are attracted to the intensity minima or maxima by the optical dipole force. In ultracold atom applications, flat-top beams can lessen the undesirable effects of spatial inhomogeneities by creating an optical lattice in which the potential wells are of uniform depth, and beams with

other precisely controlled profiles could be used to add a desired potential field variation to the optical lattice.

Our objective is to create a well-controlled laser beam to form the standing wave optical lattice potential for ultracold atom experiments. In this case, our primary interest is in achieving the highest possible level of intensity flatness over the central region. A flat phase front over the flat-top region is also required to establish a uniform optical standing wave field. The transition region and wings of the beam are less important as the cold atoms ideally never see this region and remain confined in the lowest potential region. In our application, we can sacrifice some degree of conversion efficiency from the input Gaussian profile beam to the desired profile to achieve a high degree of beam shape control and a minimum RMS deviation from the targeted beam shape. In practice, a conversion efficiency of 25%–50% with a peak power of 25%–50% of the input Gaussian beam is sufficient, provided the other criteria are met.

For ultracold atom experiments, an ultimate intensity flatness of the order of 0.1% RMS is desired. To achieve this level of beam intensity control, we have proposed a three-step development process. In the first step toward this goal, we wanted to get as close as possible to 1% RMS error in a flat-top beam by using an accurate initial measurement of the input Gaussian beam and a good design algorithm for the beam shaper. [4] Having accomplished this first step, we now consider iterative refinement of the beam based on repeated measurements of the beam profile, combined with refinement of the beam profile after each measurement. At each step of the refinement process, intensity peaks are suppressed and valleys are lifted to achieve a more accurate profile. This is the subject of this paper, where we report achieving beams with controllable intensity profiles having less than 0.25% RMS error. In the third and final step, we will image the cold atom distribution, which is even more sensitive to small variations in the optical field, and use this information to make iterative adjustments to the beam profile.

We have chosen the transmissive optics approach to beam shaping. The modulator is a digital micromirror device (DMD), Texas Instruments (TI) DLP binary-amplitude spatial light modulator (SLM). We pass the light reflected from this SLM through an imaging system containing a pinhole that acts as a spatial-frequency, low-pass filter (LPF). This system is expected to give a reasonably uniform phase and can control the light transmission in a programmed way. Adapting the technique of Dorrer and Zuegel [5], and adding further iterative pattern refinement [4], we design a DMD reflectance function that will produce the required beam shape after spatial filtering. Following this, an iterative process is used to refine the beam profile based on repeated accurate measurements of the spatial profile and adjustments to the DMD pixel pattern. This paper begins in Section 2 with a summary of the previously reported technique to produce flat-top beams and the results that we obtained. In Section 3, experimental details of the beam profiles, the experimental setup and measurement techniques, and the iterative beam refinement algorithm are given. The experimental results for two laser wavelengths, 633 and 1064 nm, are presented in Section 4, and these results are compared to simulations and the performance is evaluated in Section 5. A short summary follows in Section 6.

2. Digital Micromirror Device Beam Forming and Previous Results

Recently, we presented a DMD-based optical beam-shaping system for producing flat-top beams. [4] In this system, the input He–Ne laser beam (633 nm) was collimated and expanded by a 5× telescope to effectively illuminate the DMD face (14 mm× 10.5 mm). By using a beam splitter, a camera was placed at an equivalent plane to the DMD face and the input quasi-Gaussian beam profile was recorded. After reflecting from the DMD, the spatially modulated beam passed through an imaging telescope with a pinhole at the back focal plane of the first lens. A windowless Spiricon camera was used to accurately image the output flat-top beam.

The Floyd–Steinberg error diffusion algorithm and weighting coefficients [6] were used to design the initial DMD pixel pattern based on the measured input beam profile. This pattern was iteratively refined by simulating the optically low-pass filtered DMD image and changing the DMD pixels accordingly. This procedure is shown in the top half of the flow chart in Fig. 1. Once the DMD pattern was designed, the input Gaussian was aligned coarsely with the DMD pattern by an optical cross-correlation technique. Fine alignment was conducted by micrometer adjustments of the DMD in the x and y directions while monitoring the corresponding RMS error in the flat-top region by using Spiricon laser beam diagnostics.

This DMD-based imaging optical system converted the noisy, non-spatially filtered input beam to an eighth-order super-Lorentzian flat-top laser beam with both intensity and phase flatness. Experimental results showed 1% RMS flatness in the central region and 1.5% RMS flatness over the whole flattop for the intensity uniformity. Based on a Michelson interferometric measurement of the flatness of the central region of the DMD face and an optical analysis of the imaging telescope [4], we inferred a less than 0.8π phase difference across the output flat-top beam.

We noted the gap between the experimental result of 1.4% RMS error (for diameter = 310 camera pixels) and the simulated result for the same DMD pattern of 0.3% RMS variation. This represents 1.37% RMS additional error in the experiment that may be attributed, at least in part, to a nonoptimum DMD pattern. Therefore, it is necessary to introduce iterative refinement based on actual measurements of the output image to further improve the uniformity of the beam.
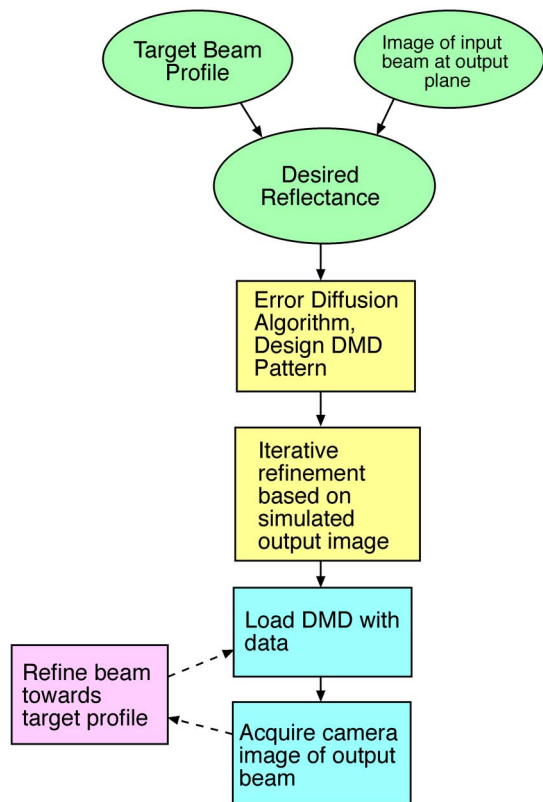
Fig. 1. (Color online) Flowchart of the DMD pattern-design algorithm.

3. Experimental Method for Beam Shaping

A. Beam Profiles Generated

To demonstrate the flexibility of our beam-shaping method, we have implemented several different target functions from the general classes of flat-top functions and sloping functions. A top-hat or perfect circle function (Circ function) profile might be an ideal flattop, but it is impractical to achieve due to its extremely high spatial-frequency bandwidth. Thus, various shapes, such as higher-order Gaussian and Lorentzian functions or cosine tapers, have been used to achieve a transition region between the flat central region and zero irradiance within a finite spatial-frequency bandwidth. The target flat-top function used in the work reported here is an eighth-order super-Lorentzian. A similarly shaped Circ function with a cosine taper was also successfully.[4] The cosine taper may be more practical for applications requiring that the flat-top function go to zero at a specified radius. We observed that these target functions showed no significant difference in RMS flatness if they had a similar spatial-frequency bandwidth. The transverse shape was varied by generating eighth-order super-Lorentzian beams of both circular and square cross sections.

In ultracold atom experiments, other beam profiles besides flat-top beams will be useful to generate various potential functions. For example, a linearly tilted laser beam profile can compensate for the ef-

fect of gravity on the atoms. As a result, we also generated square and circular cross-section, linearly tilted target functions. These functions were created by multiplying a square or circular eighth-order super-Lorentzian by a one-dimensional linearly tilted mask function.

B. Experimental Setup

The experimental setup is shown in Fig. 2. The experiment was first conducted using a 633 nm He–Ne laser and a 5× beam expander. For this wavelength, the DMD imaging telescope had a magnification of −5/6 and used 300 and 250 mm focal length lenses for $f1$ and $f2$, respectively. The pinhole diameter was 610 μm. Later, due to the need to use a wavelength of 1064 nm for the ultracold atom experiments, we used a 1064 nm fiber laser oscillator from NP Photonics with the same 5× beam expander. The imaging telescope magnification was changed to −4/5, and the two lenses were focal lengths of 500 and 400 mm. The pinhole diameter was changed to 1.2 mm. The magnification change was made to accommodate the slightly larger beam diameter incident on the DMD, and the pinhole was changed to accommodate both the changed beam size and the new wavelength. In both cases, the pinhole cutoff frequency was just sufficient to pass the target beam profile. The high spatial frequencies eliminated by the pinhole were more than 35 dB below the peak of the spectrum and, thus, were not significant in forming the beam profile. A digital LPF with an equivalent cutoff frequency to the pinhole was applied to the camera images (as described later in this section).

Compared to the previously published method, we have developed an alignment technique that simplifies both the optical setup and the alignment procedure. Previously, a 45° mirror was used to create an equivalent plane to the DMD at which to precisely measure the input Gaussian. However, since the system is an imaging telescope, we can also use the telescope output (with all the DMD pixels set to one and without a pinhole) to measure the input beam profile. This image is not as precise as for the previous setup due to the larger number of optical elements in the path and the use of scaling factors. In fact, although the initial flat-top beam produced by this setup has somewhat larger RMS error, the new iterative image
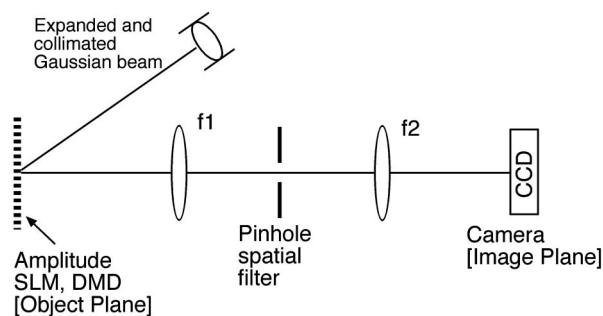
Fig. 2. Experimental setup.

correction process reduces the error to an unprecedented level. With this modified optical setup, no physical movement of optical components needs to be made during the final optimization of the DMD pattern and the utilization of the system, except for pivoting the pinhole into and out of the optical path on a kinematic arm.

To accurately measure the beam profiles, we used the Scorpion SCOR-20SOM camera manufactured by Point Grey Research, Inc. that was prepared by Spiricon, Inc. to be windowless and used with Spiricon laser beam diagnostic software. The absence of the protective window minimizes fringes or diffraction patterns caused by parallel surfaces and dirty spots. The Scorpion camera uses the Sony ICX274AL black-and-white CCD chip with $4.4\,\mu m$ square pixels in a 1600×1200 array. Relevant parameters for the camera are [7]: $QE = 0.33$ at $633\,nm$ and $QE = \sim0.01$ at $1064\,nm$, full well capacity is 8000 electrons, digitization is 12 bits (digital number, $DN = 4096$), and spatial gain noise is specified to be $<0.8\%$ RMS, and measured to be between 0.6 and 0.7% over the region of interest for the beam profiles using an incoherent, white-field image. The images generally had a peak intensity of $DN = 3100$, and 32-frame averaging was used.

Analysis of the noise sources in the images suggested that further processing might be useful. Therefore, the images were low-pass filtered using a circular (Circ function) frequency domain digital filter whose cutoff frequency was equal to the cutoff frequency of the pinhole spatial filter in the experiment. Its cutoff frequency is specified as a fraction of the maximum spatial frequency in the digital Fourier transforms of the camera images (1/32 and 1/96 for the wavelengths 633 and 1064 nm, respectively). Since the spectrum at the filter cutoff is 30 to 40 dB below the peak, we were assured that no major frequency component of the beam profile was removed. From a physical viewpoint, spatial frequencies above this frequency cannot be passed through the pinhole to the focal plane of the lens where the camera is located and, thus, must result from other noise sources.

Although the photon noise is less than 0.13% RMS at 633 nm and 0.06% RMS at 1064 nm with 32-frame averaging, there are more significant noise sources in the raw camera images. Typically a good image of a flat-top beam had RMS error between 1.0 and 1.6%. White frame measurements indicated that around 95% of the noise power was fixed pattern noise and could be corrected for the incoherent white frame, but the laser beam images contained a significant fraction of coherent interference or speckle noise that could not be corrected. A wave scattered from the camera aperture or the CCD structure that is 10^{-3} of the amplitude and 10^{-6} of the power of the incident wave can interfere with the incident wave to produce fringes with 0.14% RMS variation. Fortunately, both of these noise sources are concentrated in the high spatial frequencies, and the digital low-pass filtering process does much to reduce their
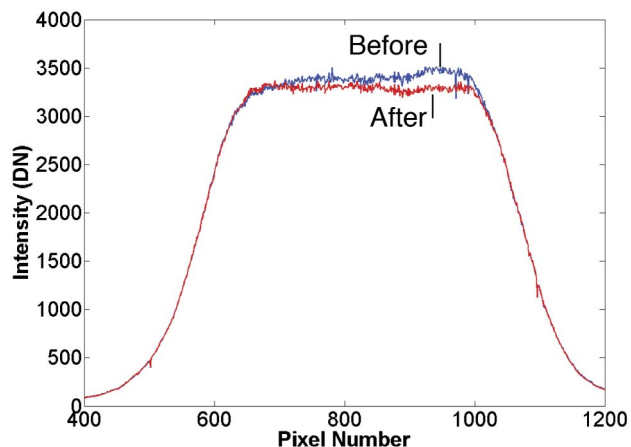
Fig. 3. (Color online) Cross section of the flat-top beam through the highest peak before and after the iterative refinement process.

contribution in the beam profile measurements. Both the pinhole and the equivalent digital filter have been adjusted to match the spatial-frequency content of the target beam profile. Thus, they cause very little distortion of the output beam from the target profile. Further, the digitally filtered beam measurements reported in Section 4 have a remaining error of between 0.2% and 0.7% RMS depending on how well the DMD pixel design was performed. An analysis of this remaining noise will be reported in Section 5. For the tabulated experimental results, both the RMS variation for the raw image and for the digitally filtered image will be given.

C. Iterative Refinement of the Beam Profile

The iterative refinement process begins with an output image (see the lower half of the flow chart in Fig. 1). An inner loop that suppresses peaks and lifts valleys uses this image after it has been digitally low-pass filtered. The intensity mean is calculated over the flat-top region of interest. For a linearly tilted intensity profile, a fitted plane function is used instead of the mean.

The inner loop operates on one peak–valley pair per loop iteration. The square areas around the peak
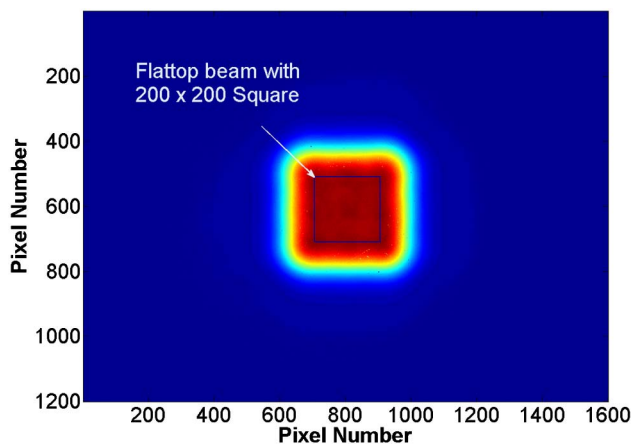
Fig. 4. (Color online) Camera image of the square flat-top beam.

Table 1. Measured Root-Mean-Square Error for the Initial Flat-Top Beam and After the Fifth Refinement Iteration versus Diameter for a Circular Flat-Top Beam at 633 nm Wavelength

Dia. (pixel)		64	126	196	286	310	324[a]
Dia. (mm)		0.28	0.55	0.86	1.26	1.36	1.43
RMS Error %	Initial	1.0	1.1	1.2	1.3	1.4	1.5
	5 iterations	0.93	0.90	0.93	0.96	1.00	1.06
	LPF[b]	0.61	0.52	0.57	0.60	0.67	0.77

[a]The diameter of 324 pixels (1.43 mm) is slightly outside the flat-top boundary.
[b]After digital LPF at 1/32 of the maximum spatial frequency.

and valley are then excluded from further processing by a bookkeeping routine. The bookkeeping routine is reset for each outer-loop iteration when a new output image is acquired with the refined DMD pixel pattern.

At the beginning of each iteration, the intensity maximum (peak) and minimum (valley) are found, and the size and shape of the peak and valley are considered to determine the area for the measurement. A square measurement area centered on the maximum or minimum coordinate with a size comparable to the peak or valley is defined. In this measurement area, the total light intensity with the respect of the area is integrated and the number of ON pixels is summed. Based on the ratio of the integrated intensity to the integrated mean intensity, the number of pixels that needs to be changed (from ON to OFF for a peak or from OFF to ON at the valley) can be calculated by

$$N = \left(1 - \frac{\int_{M.A.} I_{\mathrm{mean}} \mathrm{d}S}{\int_{M.A.} I \mathrm{d}S}\right) \times N_{\mathrm{ON}}, \qquad (1)$$

where the two integrals represent the integrated mean intensity (numerator) and integrated light intensity (denominator) and N_{ON} is the number of ON pixels in the measurement area (M.A.). A negative value for N gives the number of pixels to be turned OFF, while a positive value gives the number of lifted pixels to be turned ON.

These pixels are then changed at random locations within the measurement area following a Gaussian distribution centered at the peak (or valley) coordinate. This assures that more pixels will be changed near the center of the peak (or valley) than near the edge. Thus, the changes made to the DMD pixels fit the general shape of the peak or valley to be corrected.

After each peak–valley pair is processed, their measurement areas are set to the intensity mean to distinguish the processed region. The inner loop terminates when the entire flat-top area has been set to the mean value. This step outputs a refined DMD pattern that produces a new flat-top beam. Another camera image is taken and the process is repeated with smaller measurement areas. After each image acquisition step, the local peak–valley pairs have smaller area with improved intensity uniformity. Therefore, the measurement area needs to shrink to better match the shape of the peaks and valleys. In our experiment, the width of the square measurement area decreases from 60 to 20 pixels as the process proceeds. The whole process ends when the next iteration obtains a worse RMS error than the previous one.

4. Experimental Results

A. Beam Shaping at 633 nm

To demonstrate the flexibility of the system, we implemented circular and square eighth-order super-Lorentzian profiles at 633 nm. In this case, the raw camera image was used for the iterative refinement process without low-pass filtering. The RMS flatness for the first-generation circular flat-top beam and the beam after the fifth refinement iteration are compared in Table 1. Refinement reduced the RMS error from 1.5% to 1.0%. After the digital LPF, the error was reduced to 0.67% RMS over the flat-top region. Figure 3 displays a horizontal cross section through the highest peak of a typical circular flat-top beam without refinement superimposed on the same cross sections after five refinement iterations. As shown in the figure, the operation of the refinement algorithm successfully adjusts the peaks and valleys adaptively.

Table 2. Measured Root-Mean-Square Error for the Square Flattop versus Width for 633 nm Wavelength

Square Width (pixel)		30	50	100	160	200	240[a]
Square Width (mm)		0.13	0.22	0.44	0.70	0.88	1.06
RMS Error (%)	Initial	0.96	1.00	1.10	1.20	1.39	1.73
	5 iterations	0.81	0.89	0.89	0.86	0.90	1.19
	LPF[b]	0.48	0.55	0.61	0.56	0.61	1.00

[a]The width of 240 pixels (1.06 mm) is slightly outside the flat-top boundary.
[b]After digital LPF at 1/32 of the maximum spatial frequency.
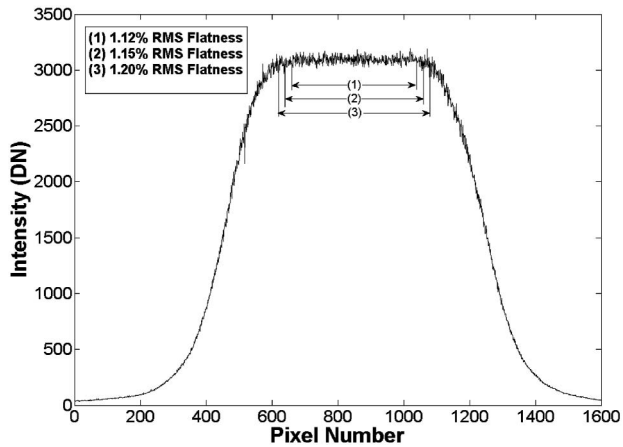
Fig. 5. Horizontal cross section of the flat-top beam at 1064 nm after five refinement iterations. Arrows indicate the diameter within which the error is below the indicated level.

Fig. 6. (Color online) Cross section and top view (inset) of the square tilted flat-top beam.

The square flat-top beam experiment yielded similar results for RMS error, as shown in Table 2. The RMS error was 0.9% over the 1.39 mm square flat-top region. When digitally low-pass filtered, the error was reduced to 0.61% RMS for the same region. A camera image of the resulting square beam is shown in Fig. 4.

B. Beam Shaping at 1064 nm

For beam shaping at 1064 nm, we updated the refinement process to use the low-pass filtered camera image to eliminate spurious responses due to isolated noise peaks. The experiment achieved 1.12% RMS flatness after refinement of the circular flat-top region. The sizes of the regions with noise below a specified level are shown in Fig. 5. The RMS error of the raw image and the digitally low-pass filtered image are given in Table 3. It is notable that the RMS error across the whole flattop was reduced to 0.23%.

Table 4 summarizes the RMS error data the over the entire flat-top region for all the tabulated experiments, with and without the digital LPF, and at both 633 and 1064 nm. Although the improved refinement process used for the 1064 nm experiments decreased the RMS error in the digitally filtered image by a significant factor, the unfiltered result was similar for both cases. This indicates that other noise sources at high spatial frequency (e.g., coherent interference and speckle noise) dominate the uniformity of the light intensity in the raw camera image.

An additional experiment was conducted to produce a beam profile that was a linearly tilted flattop that will be useful for gravity compensation in the ultracold atom experiments described in Subsection 3.A. Both circular and square cross-section, tilted flat-top beams were implemented with similar performance. A sample image of the square cross-section beam is shown in Fig. 6. This experimental result had 1.19% RMS error in the raw camera image and 0.45% RMS error after applying the digital LPF.

5. Performance Comparisons

A detailed comparison of other methods for producing flat-top beams was given in our earlier paper [4]. The best simulated performance was achieved by Dorrer and Zuegel by using the error diffusion algorithm to design a metal mask followed by a pinhole LPF [5]. They achieved 0.7% RMS error in a simulation. The best previous experimental result produced 5% RMS error in a flattop using aspheric lenses to reshape a Gaussian input beam [8]. By using the more flexible DMD-based optical system, we reported producing 1.5% RMS error without any iterative refinement. In this current work, employing iterative refinement of the DMD pixel pattern based on the output image has reduced the RMS error to <1% in the camera image and <0.25% in the spatial bandwidth of the light beam.

To determine the ultimate performance of the DMD-based optical beam-shaping system, we will analyze the various error sources in the pattern

Table 3. Measured Root-Mean-Square Error for the Initial Circular Flat-Top Beam and After 17 Refinement Iterations versus Diameter at 1064 nm Wavelength

Dia. (pixel)		52	120	230	340	376	422[a]
Dia. (mm)		0.23	0.53	1.01	1.50	1.65	1.86
RMS Error (%)	Initial	1.70	1.60	1.50	1.60	1.70	1.80
	17 iterations	1.08	1.13	1.11	1.12	1.12	1.15
	1/96 LPF[b]	0.17	0.30	0.25	0.23	0.23	0.24

[a]The diameter of 422 pixels (1.86 mm) is slightly outside the flat-top boundary.
[b]The radius of the digital LPF is 1/96 of the maximum spatial frequency.

Table 4. Summary of Root-Mean-Square Error in the Whole Flat-Top Beam Area for Three Cases Studied

Flat-Top Case	RMS Error After Feedback	RMS Error After Digital LPF[a]
Circle (dia. = 310 pixel) 633 nm	1.00	0.67
Square (width = 200 pixel) 633 nm	0.90	0.61
Circle (dia. = 376 pixel) 1064 nm	1.12	0.23

[a]The radius of the digital LPF is 1/32 and 1/96 of the maximum spatial frequency for the 633 and 1064 nm measurements, respectively.

generation and measurement processes. As part of the DMD pattern-design algorithm, the propagation of the measured input beam profile reflected from the DMD face and passed through the spatial filter optical system is simulated. This is the top portion of the flow chart shown in Fig. 1. An iterative refinement routine is run to convergence to obtain the initial DMD pixel pattern. In this iterative refinement, DMD pixels corresponding to the intensity peak or valley in the simulated output beam are flipped until no further reduction of RMS error is obtained. For these simulations (run with 1064 nm beam parameters), the minimum RMS error oscillated between 0.19% and 0.31% as the flat-top level was adjusted from 33% to 45% of the peak of the input Gaussian beam. This illustrates the range of RMS error in the flattop due to bit setting errors in the DMD pattern-generating algorithm.

Next, consider the resolution available with a finite number of binary DMD pixels. In the major lobe of the point-spread function of the pinhole LPF, there are about 610 pixels at the DMD plane. The least significant bit (LSB) is 1/610, or 0.16%. If represented as a digitizer of slightly over 9 bits, the RMS error of the digitization process would be 0.29LSB = 0.05%RMS. This leaves only a little room for improving the simulated performance of the DMD design algorithm to reach this minimum.

Compare these simulations with the experimental results at 1064 nm after the digital LPF; the lowest RMS error was 0.23% (Table 3), and other measured values ranged up to 0.35%. The camera noise consists of photon noise that is 0.02% RMS before the digital LPF and is deemed negligible after this filter. Spatial gain noise is estimated to be around 0.1% RMS after the LPF, based on white frame measurements. The digital LPF has achieved the goal of eliminating much of the photon noise, spatial gain noise, and speckle noise from the flat-top image without removing spatial-frequency content that passed through the pinhole spatial filter.

After subtracting the spatial gain noise power, the remaining experimental RMS error ranges from 0.20% to 0.34% RMS. This is in agreement with the results from the simulation for the residual RMS error in the flat-top beam (0.19% to 0.31%). For the number of DMD pixels contained within the flat-top beam, the RMS error may only be sup-

pressed to around 0.1% to 0.2%. Although illuminating more DMD pixels would result in a smaller LSB and better performance from the iterative optimization routines, this would also illuminate the more curved portion of the DMD face and introduce more astigmatism and phase nonuniformity in the beam. If the beam diameter were increased by 1.4 times, the number of pixels would double and, thus, the expected RMS error would decrease by 1/2. We conclude that, at a measured RMS error of 0.23%, we are very near the ultimate performance possible of around 0.1% RMS error.

An estimate of the power conversion efficiency at 1064 nm is the product of the mirror reflectivity (∼92%), antireflection coating transmission (∼78% for four surfaces), the fraction of DMD area active for diffraction (side/pitch)^4 = ∼74%, the diffraction efficiency to the fourth order (100% down to ∼16%, depending on DMD tilt angle and wavelength), and the fraction of the *transmitted* quasi-Gaussian function that is converted to the flattop (typically 40% in our experiments). The calculated result is in the range of 26% to 3%. For a DMD tilt angle of exactly 12°, the calculated efficiency is 11% when converting 40% of the transmitted Gaussian to a flattop. The measured result was around 7%, indicating that the actual DMD mirror tilt angle was less than 12° (but within its 11–13° specification and 45° to the square side). In comparison, a DMD tilt angle 13° at 1064 nm with a pitch of 13.68 μm would yield maximum diffraction efficiency and a total conversion of 26%.

6. Summary

We have demonstrated the ability to shape non-spatially filtered laser beams into beams with precisely controlled profiles that have an unprecedented level of RMS error with respect to the target profile. Based on our experimental results, we have demonstrated that our iterative refinement process of the beam profile that uses output images is able to improve the light intensity uniformity down to around 1% RMS error in a raw camera image for both red and infrared laser beams. The use of a digital LPF on the camera image is justified in that it matches the performance of the pinhole filter in the experimental setup. The digital LPF results reveal that the actual optical beam profiles have RMS error down to 0.23%. In addition, our approach demonstrated the ability to produce a range of target profiles as long as they had similar spatial-frequency content (i.e., slowly varying beam profile). Circular and square cross-section flat-top beams and beams with a linear intensity variation within a circular and square cross section were produced with similarly low RMS errors. The measured errors were about twice the ultimate limit based on the number of binary DMD pixels that participate in the beam-formation process. These results indicate that this beam-shaping technique performs sufficiently well

to be used to form the standing wave optical lattice in ultracold atom experiments.

References

1. M. G. Tarallo, J. Miller, J. Agresti, E. D'Ambrosio, R. DeSalvo, D. Forest, B. Lagrange, J. M. Mackowsky, C. Michel, J. L. Montorio, N. Morgado, L. Pinard, A. Remilleux, B. Simoni, and P. Willems, "Generation of a flat-top laser beam for gravitational wave detectors by means of a nonspherical Fabry–Perot resonator," Appl. Opt. **46**, 6648–6654 (2007).
2. M. Takamoto, F. L. Hong, R. Higashi, and H. Katori, "An optical lattice clock," Nature **435**, 321–324 (2005).
3. E. Jane, G. Vidal, W. Dur, P. Zoller, and J. I. Cirac, "Simulation of quantum dynamics with quantum optical systems," Quantum Inf. Comput. **3**, 15–37 (2003).
4. J. Liang, R. N. Kohn, M. F. Becker, and D. J. Heinzen, "1.5% root-mean-square flat-intensity laser beam formed using a binary-amplitude spatial light modulator," Appl. Opt. **48**, 1955–1962 (2009).
5. C. Dorrer and J. D. Zuegel, "Design and analysis of binary beam shapers using error diffusion," J. Opt. Soc. Am. B **24**, 1268–1275 (2007).
6. R. W. Floyd and L. Steinberg, "An adaptive algorithm for spatial grey scale," Proc. Soc. Inf. Disp. **17**, 75–77 (1976).
7. Basler, "A641f Camera Specification, Measurement protocol using the EMVA Standard 1288" (Basler Vision Solutions AG, 2007).
8. J. A. Hoffnagle and C. Michael Jefferson, "Design and performance of a refractive optical system that converts a Gaussian to a flattop beam," Appl. Opt. **39**, 5488–5499 (2000).